We are IntechOpen, the world's leading publisher of Open Access books Built by scientists, for scientists

4,800
Open access books available

122,000
International authors and editors

135M
Downloads

Our authors are among the

154
Countries delivered to

TOP 1%
most cited scientists

12.2%
Contributors from top 500 universities

WEB OF SCIENCE™

Selection of our books indexed in the Book Citation Index in Web of Science™ Core Collection (BKCI)

Interested in publishing with us?
Contact book.department@intechopen.com

Numbers displayed above are based on latest data collected.
For more information visit www.intechopen.com

Chapter 37

Stress Intensity Factor Determination for Three-Dimensional Crack Using the Displacement Discontinuity Method with Applications to Hydraulic Fracture Height Growth and Non-Planar Propagation Paths

Farrokh Sheibani and Jon Olson

Additional information is available at the end of the chapter

http://dx.doi.org/10.5772/56308

Abstract

Stress intensity factor determination plays a central role in linearly elastic fracture mechanics (LEFM) problems. Fracture propagation is controlled by the stress field near the crack tip. Because this stress field is asymptotic dominant or singular, it is characterized by the stress intensity factor (SIF). Since many rock types show brittle elastic behaviour under hydrocarbon reservoir conditions, LEFM can be satisfactorily used for studying hydraulic fracture development. The purpose of this paper is to describe a numerical method to evaluate the stress intensity factor in Mode I, II and III at the tip of an arbitrarily-shaped, embedded cracks. The stress intensity factor is evaluated directly based on displacement discontinuities (DD) using a three-dimensional displacement discontinuity, boundary element method based on the equations of proposed in [1]. The boundary element formulation incorporates the fundamental closed-form analytical solution to a rectangular discontinuity in a homogenous, isotropic and linearly elastic half space. The accuracy of the stress intensity factor calculation is satisfactorily examined for rectangular, penny-shaped and elliptical planar cracks. Accurate and fast evaluation of the stress intensity factor for planar cracks shows the proposed procedure is robust for SIF calculation and crack propagation purposes. The empirical constant proposed by [2] relating crack tip element displacement discontinuity and SIF values provides surprisingly accurate results for planar cracks with limited numbers of constant DD elements. Using the described numerical model, we study how fracturing from misaligned horizontal wellbores might results in non-uniform height growth of the hydraulic fracture by evaluating of SIF distribution along the upper front of the fracture.

1. Introduction

Stress intensity factor determination plays a central role in linearly elastic fracture mechanics problems. Fracture propagation is controlled by the stress field near the crack tip. Because the stress field near the crack tip is asymptotic dominant or singular, it is characterized by the stress intensity factor. The real stress distribution at the vicinity of crack tip and the K-field LEFM approximation can be depicted schematically as in Figure 1. The stress singularity right at the tip of the crack cannot be experienced in real nature because inelastic deformation prevents the crack tip from being perfectly sharp. However, according to small scale yielding of the process zone immediately around the crack tip in comparison with the K-field region (Figure 2), the SIF is the quantity which dictates if/when the crack will propagate. The inaccuracy of the stress field calculation using the SIF based on LEFM is less than 15% of the exact solution over the distance ranging from $r < 0.01a$ to $r < 0.15a$, where r is the radius of K-field region and a is the half length of the crack [4].

Since SIF was proposed by Irwin [5] to express displacements and stresses in the vicinity of crack tip, several analytical techniques have been developed for a variety of common crack configurations; however, these analytical solutions are limited to simple crack geometries and loading conditions. For the case of 3-D planar cracks embedded in a semi-infinite body, there are less available analytical solutions for SIF. These exact analytical solutions provide good insight about fracture problems but they are not usable for general crack propagation modeling where the geometry of simultaneously propagating cracks can be asymmetrical and irregular and the boundary conditions can be complicated. Fortunately, advances in numerical modeling procedures supported by the fast growing speed of computational calculation have opened new doors for fracture propagation analysis.

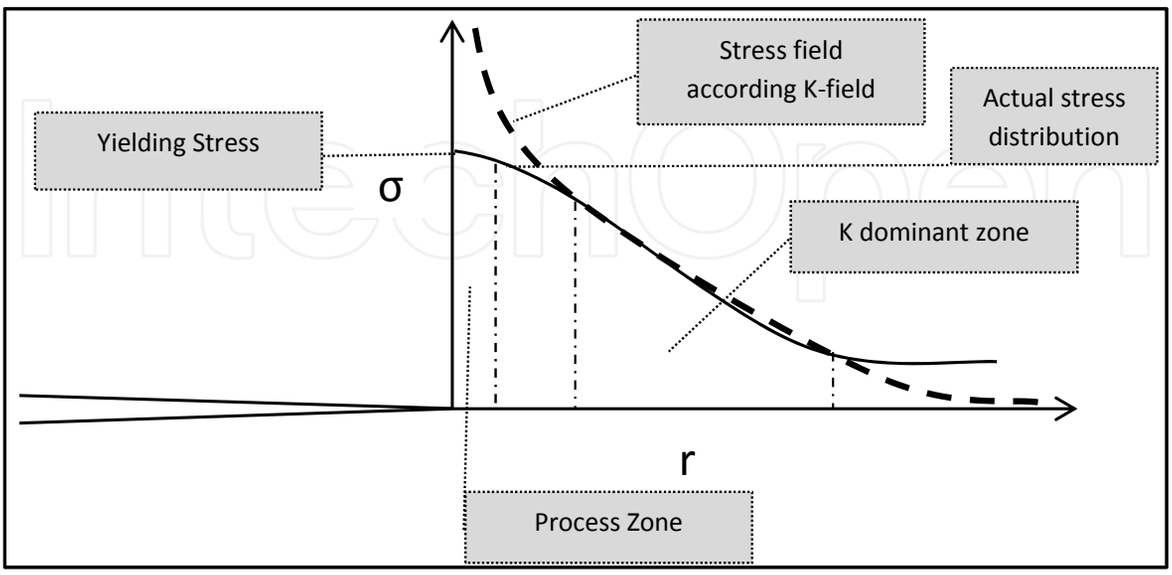

Figure 1. Schematic representation of stress distribution around the crack tip [3]

http://dx.doi.org/10.5772/56308

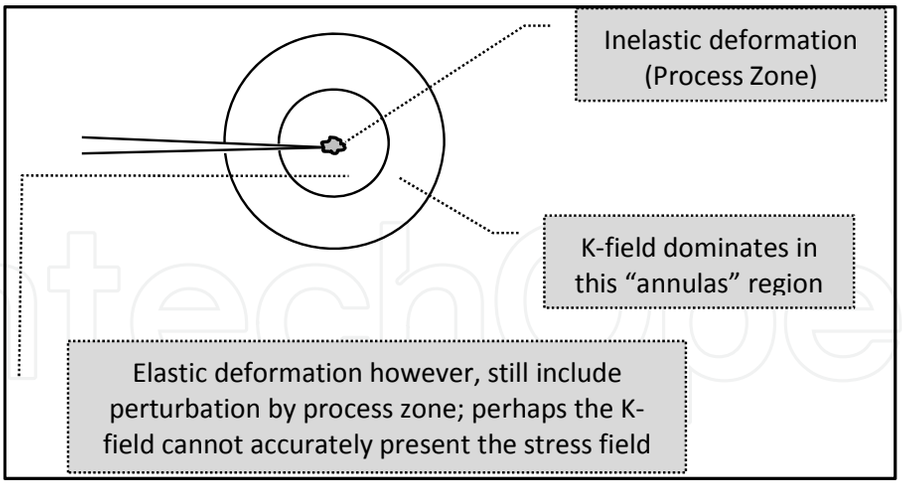

Figure 2. Process zone and K-filed representation [3]

There are four general distinctive numerical methods to model fracture propagation problems:

1. The boundary element method (BEM) requires discretization and calculation only on boundaries of the domain. The stress resolution is higher in comparison with finite element and finite difference methods because the approximation is imposed only on boundaries of the domain, and there is no further approximation on the solution at interior points. Particularly, for some problems where the ratio of boundary surface to volume is high (for instance for large rock masses), BEM can be advantageous because FEM or other whole-domain-discretizing methods require larger numbers of elements to achieve the same accuracy.

2. The Finite Element Method (FEM) has been widely used in fracture mechanics problems since it was implemented by [6] for SIF calculation. Several modifications have proposed to remove its deficiencies in LEFM problem modeling. [7] and [8] devised "quarter point element" or "singularity elements" to improve the accuracy of stress and displacement distributions around the crack and SIF evaluation. To overcome the time consuming process of remeshing in fracture propagation problems, [9] proposed the Extended Finite Element Method (XFEM). XFEM allows fracture propagation without changing the mesh by adding analytical expressions related to the crack tip field to the conventional FE polynomial approximation in what are called "enriched elements". Further work is being done ([10] and [11]) to address the accuracy and stability of XFEM modeling, especially for multiple crack problems and approaching tip elements called "blending elements".

3. The Finite Difference Method (FDM) requires calculations on a mesh that includes the entire domain. FDM usage in fracture mechanics is mostly limited to dynamic fracture propagation and dynamic SIF calculation ([12] and [13].)

4. The Discrete Element Method (DEM) is mostly applied when continuity cannot be assumed in discontinuous, separated domains. The method apply to describe the behavior of discontinuities between bodies with emphasize on the solution of contact and impact between multiple bodies [14].

Generally, when the geometry of a problem is changing, whole-domain-discretizing methods like FEM, FDM and DEM are more time-consuming than BEM because of the remeshing process around a propagation fracture. However, BEM loses its advantage when the domain is grossly inhomogeneous.

The "Integral equation" approach (also called influence function) and the "displacement discontinuity method" are two types of BEM widely used in LEFM analysis. Both approaches incorporate only boundary data by relating boundary tractions and displacements. In the integral equation technique, superposition of known influence functions (called Green's function) along boundaries generate a system of simultaneous integral equations [15]. In DDM, unknown boundary values are found from a simple system of algebraic equitation [16]. Generally, DDM has the advantage over integral equations in being faster, while integral equations can be more accurate for non-linear problems.

SIF values can be obtained from the displacement discontinuity magnitudes at crack tip elements [17-19]. However, according to [16], DDM consistently overestimates displacement discontinuities at the tip of the crack (considering element midpoint) by as much as 25%. To improve the accuracy of the solution, some researchers proposed using higher accuracy crack tip element and/or using relatively denser distribution of elements near the crack tip. [20] proposed higher order elements to improve the DDM solution and they used numerical integration to find the fundamental solution of linear and quadratic displacement discontinuities. [21] proposed another approach called "hybrid displacement discontinuity method" by using parabolic DD for crack tip elements and constant DD for other elements. He concluded increasing the number of elements more than 8-10 times cannot yield more accurate results and the error in mode I stress intensity factor calculation for a 2-D straight crack with uniform internal pressure, sporadically changes in a range of 1% to about 10% depending on the ratio of parabolic element length to constant element length. However, [22] used the same combination of DD element and concluded the ratio of crack tip element to constant DD element must be between 1-1.3 to obtain good results with relative error less than 3% in mode II SIF calculation for a straight 2-D crack. [23] presented a new hybrid displacement discontinuity method by using quadratic DD elements and special crack tip elements to show $\sqrt{r}$ variation of displacement near the crack tip. [24] used the same method with few modifications about the position of collocation points to determine quadratic elemental displacement. They showed the error can be fixed up to 1.5% for Mode I, and about 2% for mode II SIF calculation for a slanted straight crack. [25] took a different approach; instead of direct calculation of stress intensity factors from displacement discontinuities, they proposed a "equivalence transformation method" in which stresses on the crack surface are calculated from displacement discontinuities, and then by using crack line Green's function, the SIF at the crack tip can be obtained from calculated stresses. They implemented the equivalence transformation method to calculate dynamic stress intensity factors for an isolated 2-D crack in an infinite sheet subjected to Heaviside loading. By comparison with the exact solution and using 80 DD elements, they inferred the error in mode I SIF is less than 1% and for mode II doesn't exceed 1.5%.

http://dx.doi.org/10.5772/56308

All of the methods mentioned above including using special crack tip elements or equivalence transformation methods to decrease the error in crack tip element displacement and corresponding SIF calculation; however, they all need numerical integration and can be more time-consuming than constant elemental DD approximation. Ref. [2] empirically determined the coincidence between DDM modeling and analytical displacement distribution solution of a straight 2-D crack to remove the error. He showed the margin of error is less than 5% even by using only 2 elements in a 2-D crack. His proposed formula has been widely used in geologic fracture problems [26-29]. This paper extends Olson's method ion [2] to SIF calculation for 3-D homogenous, isotropic and linearly elastic material problems. [30] changed the correction constant. The empirical constant they proposed was used by some researchers afterwards ([31] and [32]), but we argue the change does not actually improve SIF accuracy.

According to Murakami and [33] and [34] the maximum mode I stress intensity factor appearing at a certain point along the crack front can be estimated by Equation (1) with less than 10% error for an arbitrary-shaped planar crack.

$$K_{I\ max} = 0.50\sigma\sqrt{\pi\sqrt{area}} \tag{1}$$

where 'area' is the area of crack projected in the direction of the maximum principal stress.

Fortunately, for simple crack geometries like elliptical and circular cracks, there exist analytical formulae for mode I stress intensity factor variation along the crack tip which help us to evaluate the accuracy of the numerical modeling ([35] and [36]). For rectangular defects there are no analytical formulae, but the accuracy of DDM numerical modeling can be examined by comparing against earlier numerical work using integral equation methods [37-40].

2. Numerical procedure

2.1. Displacement discontinuity method

The general concept of the displacement discontinuity method proposed by [16] is to approximate the distribution of displacement discontinuity of a crack by discretizing it into elements. Knowing the analytical solution for one element, the numerical elastic solution of the whole discontinuity can be calculated by adding up the effect of all subdividing elements.

The 3-D displacement discontinuity used here is based on the analytical elastic solution of normal and shear displacement of a finite rectangular discontinuity in half-space (Figure 3) proposed by [1]. These equations are closed-form half-space solutions of deformations and deformation derivatives in which most of singularities and mathematical instabilities were removed.

By placing N unknown constant displacement elements within the boundaries of the region to be analyzed and knowing the boundary conditions on each element (traction or displacement), a system of $3N$ linear algebraic equations can be set up as the following:

$$\sigma_s^i = \sum_{j=1}^{N} A_{ss}^{ij} D_s^j + \sum_{j=1}^{N} A_{sd}^{ij} D_d^j + \sum_{j=1}^{N} A_{sn}^{ij} D_n^j \quad a$$
$$\sigma_d^i = \sum_{j=1}^{N} A_{ss}^{ij} D_s^j + \sum_{j=1}^{N} A_{sd}^{ij} D_d^j + \sum_{j=1}^{N} A_{sn}^{ij} D_n^j \quad b \qquad (2)$$
$$\sigma_n^i = \sum_{j=1}^{N} A_{ns}^{ij} D_s^j + \sum_{j=1}^{N} A_{nd}^{ij} D_d^j + \sum_{j=1}^{N} A_{nn}^{ij} D_n^j \quad c$$

where N is the total number of elements, s, d, n are the directions of local coordinates depicted in Figure 3, D_s^j, D_d^j and D_n^j are unknown strike-slip shear, dip-slip shear and opening displacement discontinuities of the jth element, σ_s^i, σ_d^i and σ_n^i are known strike-slip shear, dip-slip shear and normal boundary tractions induced on the ith element, and A is the boundary influence coefficient of the stresses tensor. If known values are the displacements of one side of boundary elements, these equations will be modified as:

$$u_s^i = \sum_{j=1}^{N} B_{ss}^{ij} D_s^j + \sum_{j=1}^{N} B_{sd}^{ij} D_d^j + \sum_{j=1}^{N} B_{sn}^{ij} D_n^j \quad a$$
$$u_d^i = \sum_{j=1}^{N} B_{sd}^{ij} D_s^j + \sum_{j=1}^{N} B_{dd}^{ij} D_d^j + \sum_{j=1}^{N} B_{dn}^{ij} D_n^j \quad b \qquad (3)$$
$$u_n^i = \sum_{j=1}^{N} B_{sn}^{ij} D_s^j + \sum_{j=1}^{N} B_{nd}^{ij} D_d^j + \sum_{j=1}^{N} B_{nn}^{ij} D_n^j \quad c$$

where, u_s^i, u_d^i and u_n^i are known strike-slip and dip-slip shears and opening on the positive (or negative) face of the crack (Figure 3), and the B matrix is called the boundary influence coefficient of the displacements tensor.

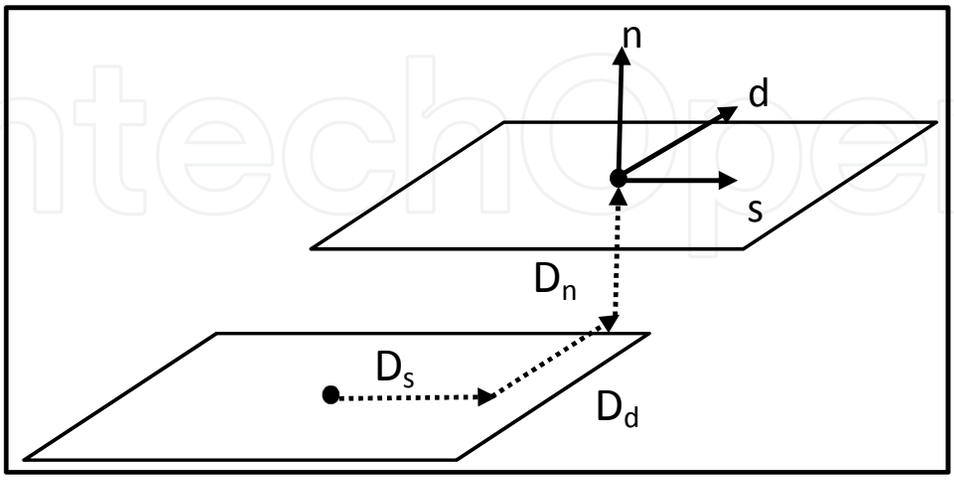

Figure 3. D displacement Discontinuity Modeling

http://dx.doi.org/10.5772/56308

2.2. Stress intensity factor computation

By knowing the crack tip element displacement discontinuities, K_I, K_{II} and K_{III} can be directly calculated using Equations 4a, b & c respectively:

$$K_I = C\frac{D_n E\sqrt{\pi}}{4(1-\nu^2)\sqrt{P}} \quad a$$
$$K_{II} = C\frac{D_s E\sqrt{\pi}}{4(1-\nu^2)\sqrt{P}} \quad b \qquad (4)$$
$$K_{III} = C\frac{D_t E\sqrt{\pi}}{4(1+\nu)\sqrt{P}} \quad c$$

where E is modulus of elasticity, ν is Poisson's ratio, P is crack tip element length perpendicular to crack front, D_n is the opening of crack tip element, D_s is shear displacement discontinuity perpendicular to D_n and the crack front, D_t is front-parallel displacement discontinuity (Fig. 3) and C is an empirically determined constant that accounts for the discrepancy between the numerical approximation and the analytical solution. [2] empirically determined that the analytical and numerical solutions for a planar 2-D crack coincide at approximately at $x = \left(a - \frac{P}{1.3}\right)$, where x is the distance from the center of the crack and a is half length of the crack. He showed by using the empirical constant $C = 0.806$ the margin of error is less than 5% for stress intensity factor calculation of a 2-D crack even when there are only two elements in a crack. The proposed modified constant of $C = 0.798$ by [30] does not improve on this accuracy.

3. Validation of numerical model

3.1. Rectangular crack

There is no analytical solution for the stress intensity factor variation along a rectangular crack front. However, rectangular cracks were the subject of several papers where the "Integral Equation" or "Body Force Method" was used to numerically approximate mixed Mode SIF values [37-42]. Results obtained from [39] are in a good agreement with [40] for maximum SIF calculation of rectangular cracks. In addition, [39] investigated how maximum stress intensity factors change in a half-space in terms of crack depth. Because of these reasons, [39] and [40] were selected as reference solutions to which we compare the results from this paper. Studies done by [37], [41] and [43] yield relatively different results for $K_{I\,max}$ calculation. These earlier works are different about 5% in average [39]. In addition they cannot be used for stress intensity factor variation along the crack edge. Equation 1 proposed by [34] is among few studies done to find the maximum stress intensity factor of an arbitrary-shaped crack. Using that formulae and knowing the maximum stress intensity factor for a rectangular discontinuity always is at the middle of longer edge, the maximum stress intensity factor of a rectangular crack can be approximated with adequate accuracy. For instance, they approximated the dimensionless

stress intensity factor at the edge-midpoints of a square crack as F_I=0.768 which the error is about 1%.

Considering a rectangular crack as shown in Figure 4, the following dimensionless parameter is proposed to demonstrate the result of stress intensity factor of a rectangular crack. F_I is called the dimensionless stress intensity factor along the crack front $y=b$:

$$F_I = \frac{K_I(x,\ y)|\ x=x,\ \ y=\pm b}{\sigma_n\sqrt{\pi b}} \tag{5}$$

The stability of the solution can be examined by investigation of the strain energy variation through increasing the number of elements. Figure 5-b shows that strain energy (U) linearly varies with $\frac{1}{n}$ and has an asymptotic behavior with respect to n, where n is the number of element on each side of a square crack shown in Figure 5-b. The area of the square crack is A under constant pressure p.Assuming the error in strain energy calculation approaches zero if $n \to \infty \left(\frac{1}{n} \to 0\right)$, the correct answer for error estimation in the strain energy calculation can be obtained from Figure 5-b. Figure 5a shows the error calculation in strain energy. The displacement discontinuity method always overestimates the strain energy (or displacement across the crack surface) but it yields more accurate results closer to the exact solution when the number of elements increases. The error changes from 48.8% using a 3×3 mesh to about 1.99% for a mesh including 71×71 elements. In comparison with the two dimensional analysis of a straight crack [16], the rate of convergence is faster, but the error in strain energy calculation is higher using the same number of elements to divide one side of a crack.

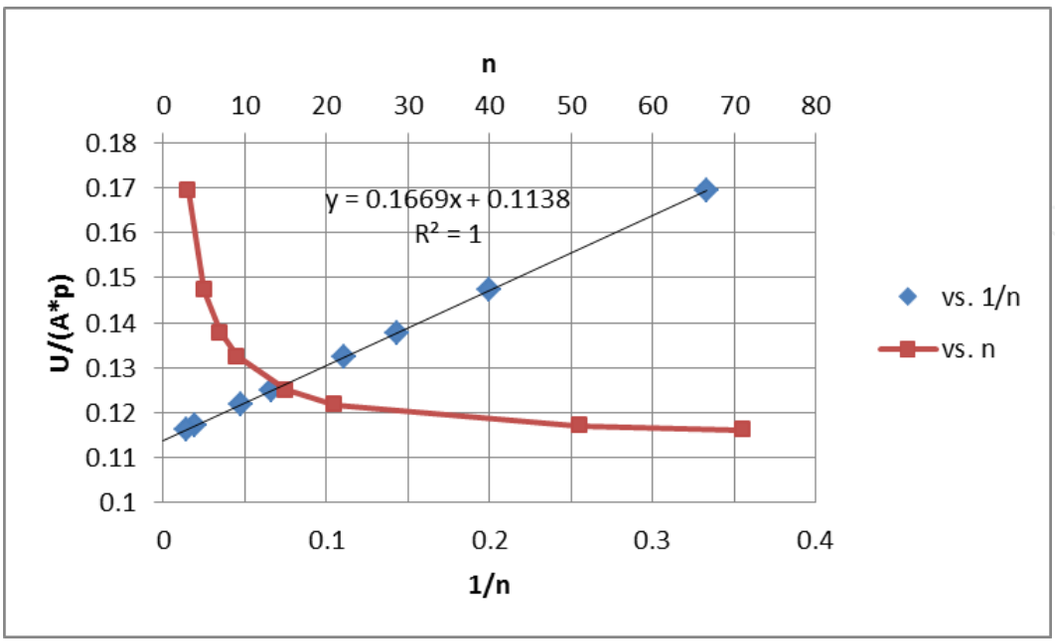

Figure 4. Approximation of the exact solution of strain energy for a square pressurized crack

http://dx.doi.org/10.5772/56308

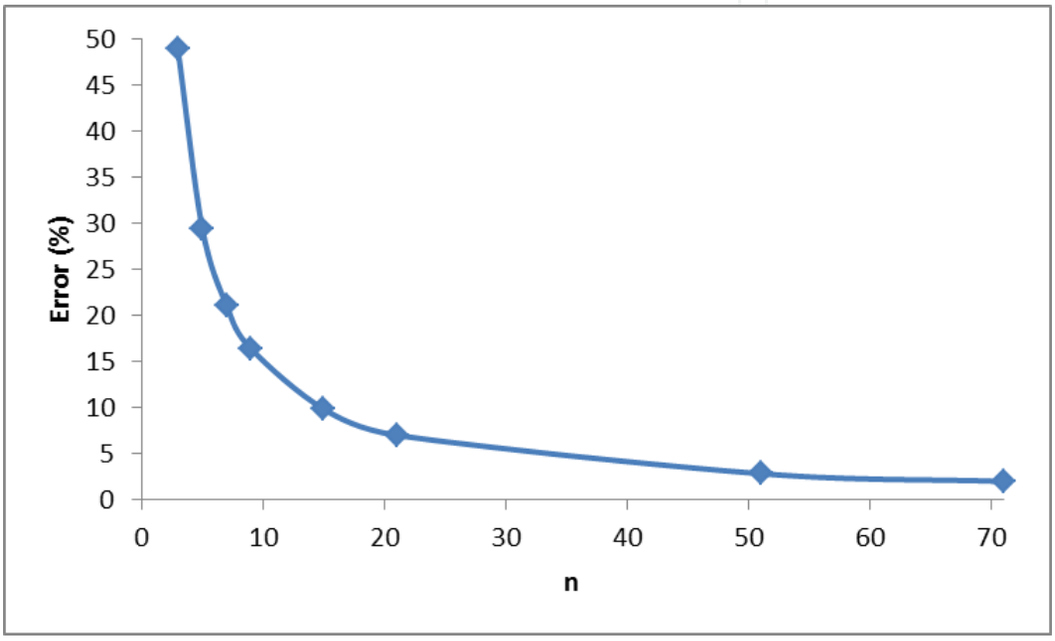

Figure 5. Error in strain energy calculation as a function of number of elements on each side of a pressurized square crack (*a*=*b*)

The error in strain energy calculation is mainly related to the largest error occurring at the corners of the square crack where the displacement gradient is highest. Figure 6 shows the stress intensity factor variation along the half-length of the crack tip using DDM compared with the integral equation solution suggested by [40]. The total number of elements used in the simulation was 22×22 to be consistent with the number of colocation points used in [40]. The difference between these two solutions is negligible for all elements but the corners (element No. 11). However, the corner elements of rectangular cracks don't play an important role in fracture propagation problems because the level of SIF is the lowest there and unlikely to control the initiation of crack propagation.

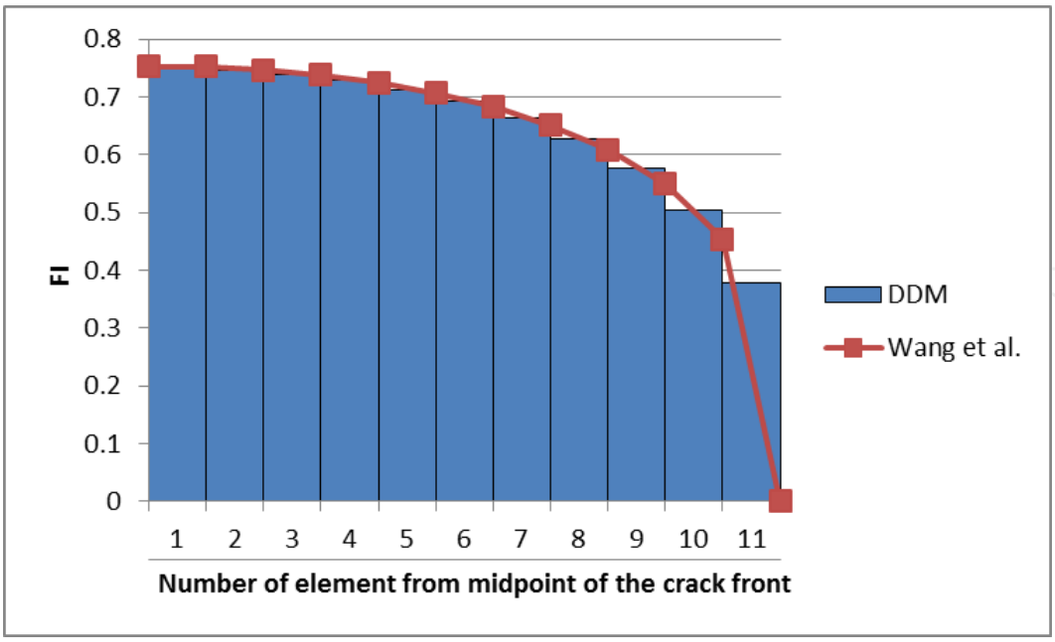

Figure 6. Dimensionless stress intensity factor variation along the half length of a square crack front

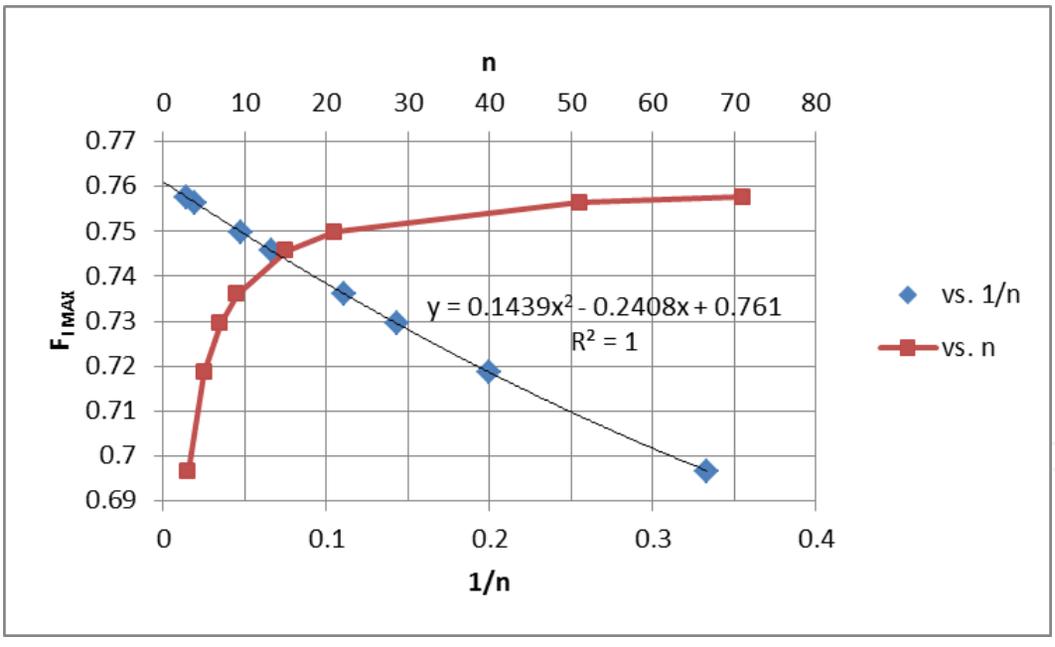

Figure 7. Extrapolation of $F_{I\,max}$ for a square crack in an infinite body

It is always desirable to use a coarser mesh to save computation time, but the accuracy of DDM depends strongly on mesh refinement. Figure 7 shows the extrapolation of maximum dimensionless stress intensity factor, $F_{I\,max}$(which occurs at side-midpoint of a square crack) as a function of $\frac{1}{n}$. It shows the numerical result of $F_{I\,max}$ is parabolic with the reciprocal of the

http://dx.doi.org/10.5772/56308

subdivision number. Figure 7 shows that the most reliable value of $F_{I\,max}$ for a square crack is 0.7607, which is slightly different (0.6%) than the value reported by [39] using body force method.

Figure 8 shows the variation of dimensionless stress intensity factor, F_1, along the crack front y=b for various values of $\frac{b}{a}$, using 22×22 elements, a mesh refinement consistent with [40]. Figure 9 shows the maximum dimensionless stress intensity factor ($F_{I\,max}$) at the location ($x=0$, $y=b$). When $b/a<1$, the crack tip at $y=b$ is represents the longer edge of a rectangular crack, whereas when $b/a>1$ the crack tip at $y=b$ represents the shorter tip. The dimensionless SIF is referenced to the plane strain SIF for a crack with half-length b for all b/a. The results show that at b/a=0.125, the maximum SIF (at location $x=0$, $y=b$) has reached the plane strain value ($F_1=1$). As b/a increases (equivalent to reducing the crack length a relative to b), F_1 is reduced. When b/a=1.0, the square crack, F_1=0.75. A penny-shaped crack has more restricted opening, and has the ratio of 0.64 to the plane strain SIF. Reducing a further such that $b/a>1$ makes a the short dimension of the crack and thus the limiting dimension for crack opening and SIF value. The SIF at y=b will then go to 0 as $a\rightarrow 0$. In comparing to the solution of [Wang et al 2001], it is evident that the distribution of SIF near the $x=a$ crack tip is more accurate when $b/a<1$, but the maximum value of SIF is a good match for all cases. Using higher element density around the rectangular crack front and a coarser mesh at the center was investigated, but we found a uniform mesh yielded more accurate results using fewer elements in comparison with non-uniform mesh.

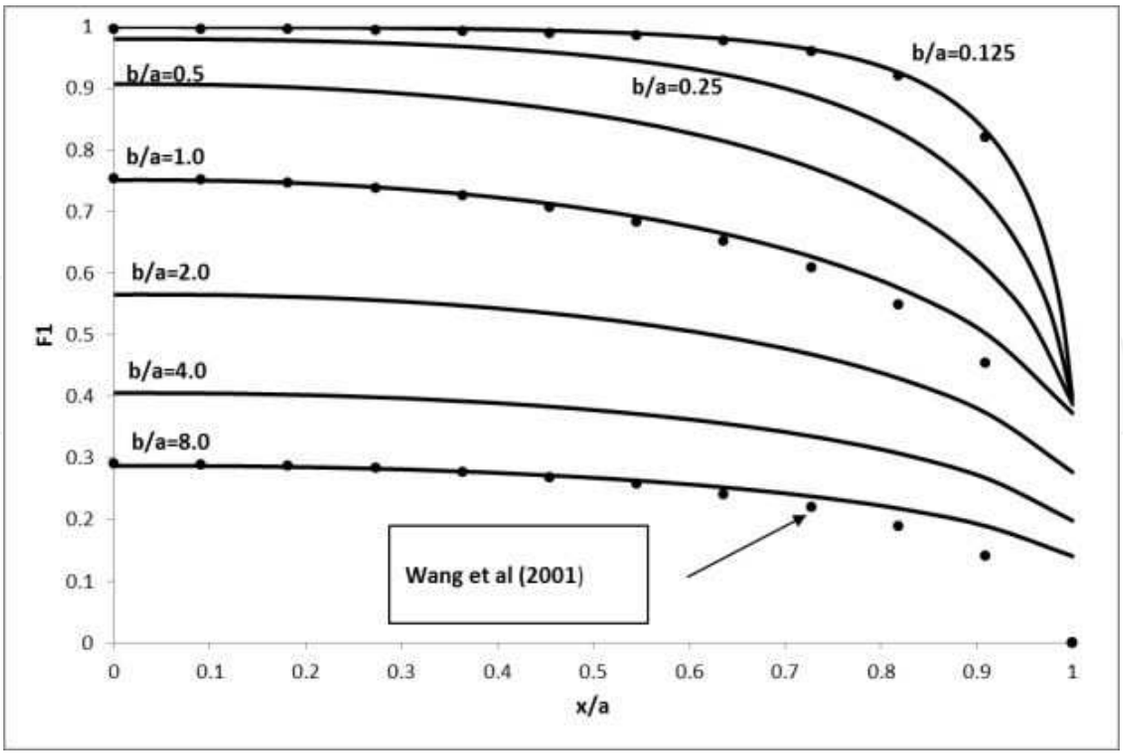

Figure 8. Dimensionless stress intensity factor variation along the crack front $y=b$.

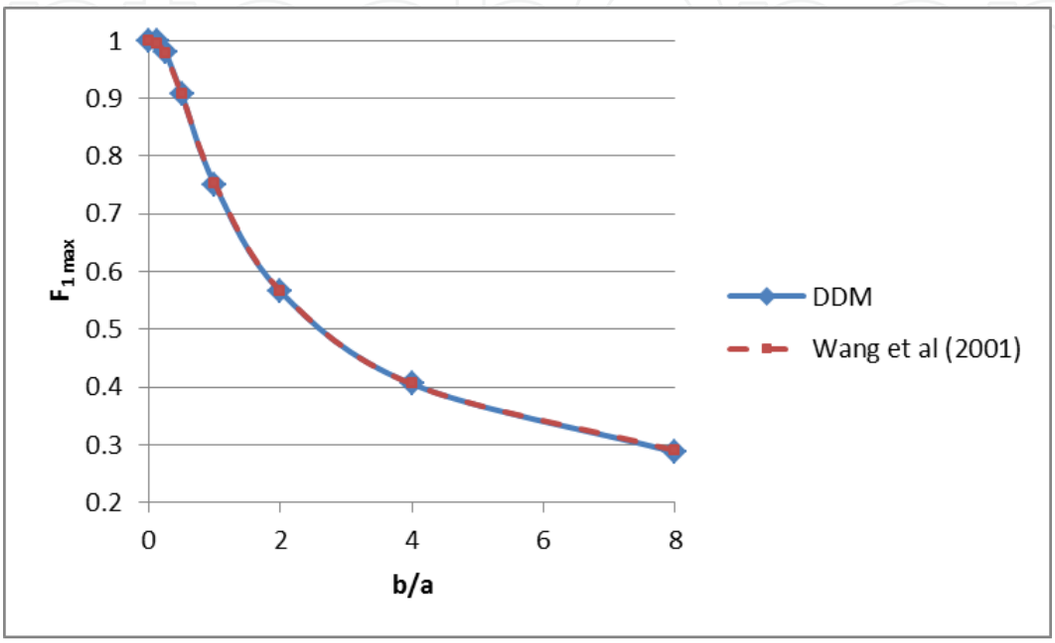

Figure 9. Maximum dimensionless stress intensity factor along the crack front $y = b$.

Considering a rectangular vertical crack in a half-space, and assuming $\nu = 0.3$, the dimensionless stress intensity factor at midpoints of crack fronts nearest (A_1) and farthest (A_2) from the free surface are presented in Figure 10a and b respectively, as a function of b/a and b/d. $F_{1\,max}$ and $F_{2\,max}$ are the dimensionless stress intensity factors corresponding to points A_1 and A_2 respectively and can be defined as the following:

$$F_{1\,max} = \frac{K_I(x,\ y)|A_1}{\sigma_n\sqrt{\pi b}}\ a$$
$$F_{2\,max} = \frac{K_I(x,\ y)|A_2}{\sigma_n\sqrt{\pi b}}\ b \tag{6}$$

where σ_n is the normal pressure at the surface of crack. For every combination of b/a and b/d, the stress intensity factor along the side nearest to the free surface is greater than the side farthest away.

http://dx.doi.org/10.5772/56308

Figure 10-a and b show for greater aspect ratio (b/agrater or taller crack) SIF is less affected by the depth. Both $F_{1\,max}$ and $F_{2\,max}$ increase as the crack approaches the surface of solid. The mode I stress intensity factor along the crack fronts of a rectangular discontinuity in an infinite body is independent of Young's modulus [45]. Figure 11a and 11b show that Poisson's ratio ν variation has a slight effect on $F_{1\,max}$ and $F_{2\,max}$, but only for cracks close to the free surface.

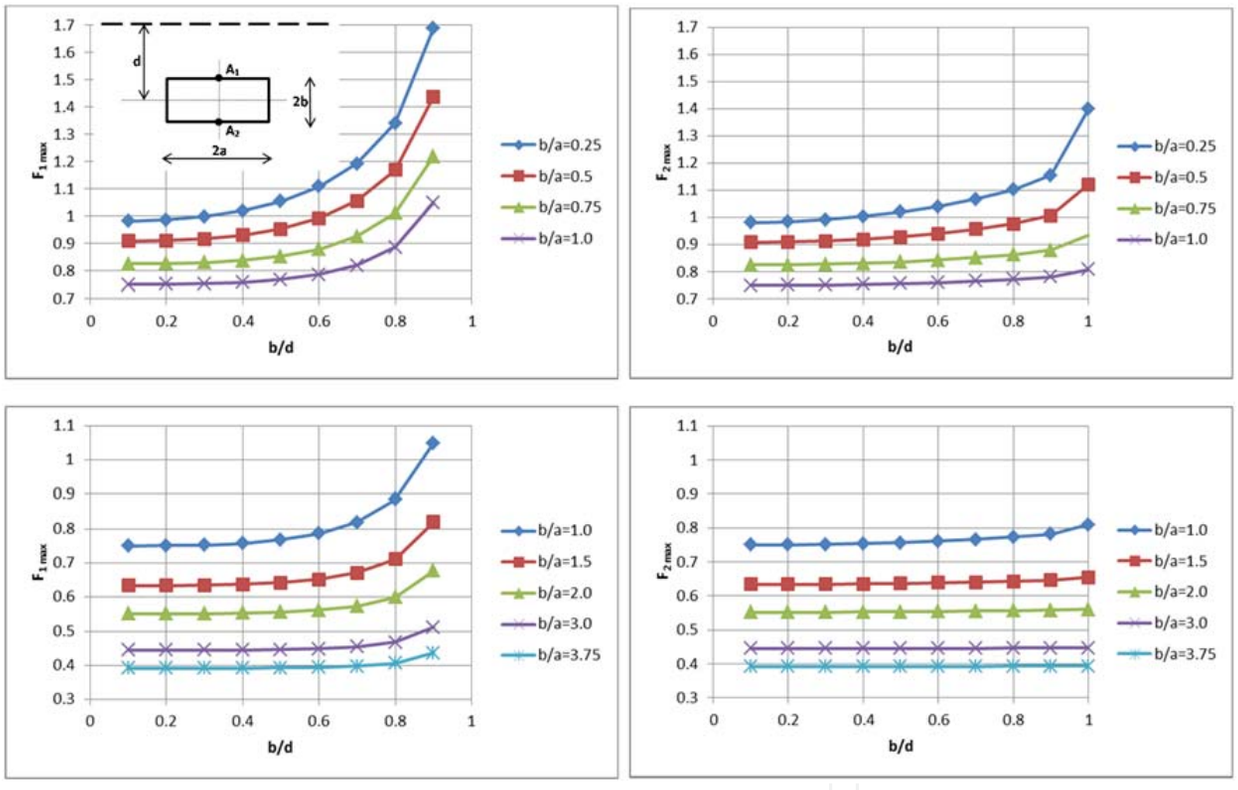

Figure 10. a Dimensionless stress intensity factor, $F_{1\,max}$as a function of b/a and b/d for a rectangular crack in half-space (ν=0.3); b Dimensionless stress intensity factor $F_{2\,max}$ as a function of b/a and b/d for a rectangular crack in half-space (ν=0.3)

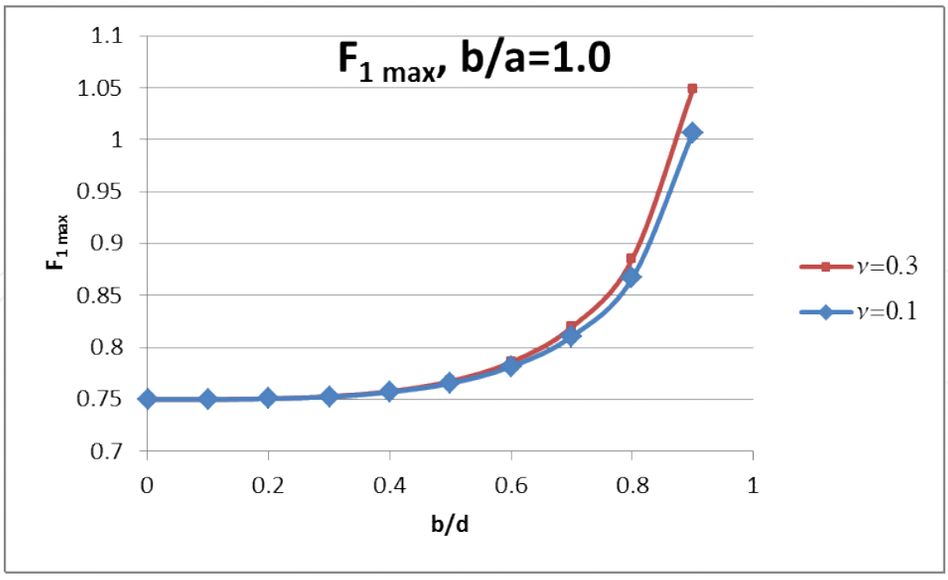

(a)

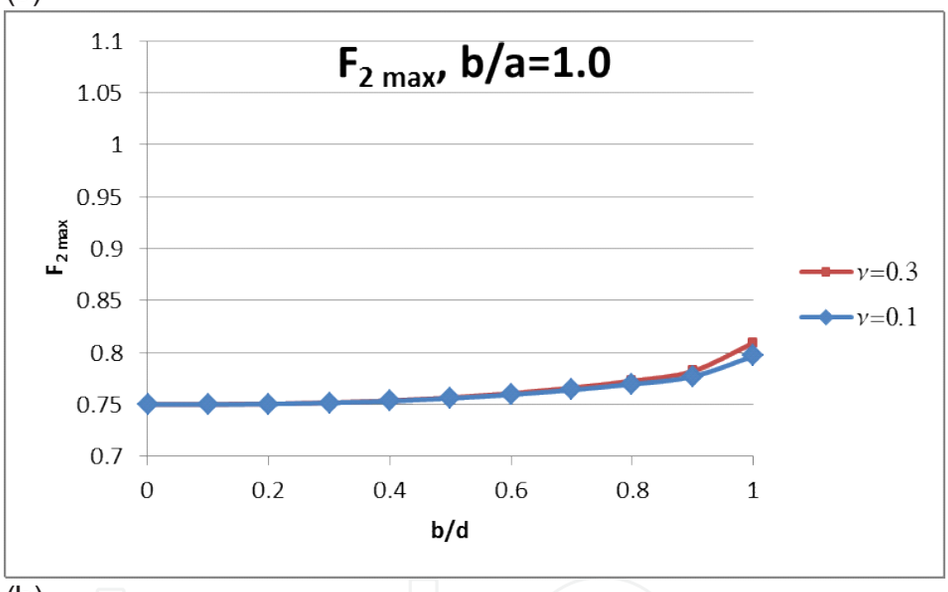

(b)

Figure 11. a. Effect of Poisson's ratio on dimensionless stress intensity factor, $F_{1\,max}$ for a rectangular crack in half-space; b. Effect of Poisson's ratio on dimensionless stress intensity factor $F_{2\,max}$ for a rectangular crack in half-space

In contrast to Mode I, for mode II and III stress intensity factor of a crack in an infinite body is dependent on elastic constants. By defining the dimensionless stress intensity factor for mode II, $F_{II} = \frac{K_{II}(x,\ y)|\,x=x,\ y=\pm b}{\tau_{zx}\sqrt{\pi b}}$ and assuming a frictionless surface crack, Figure 13 shows the maximum dimensionless stress intensity factor along the rectangular crack front $y=b$ subject to front-perpendicular shear stress τ_{zx}. The figure shows increasing Poisson's ratio will increase mode II stress intensity factor at the tip of a rectangular crack embedded in an infinite space. Results were satisfactory compared with [38].

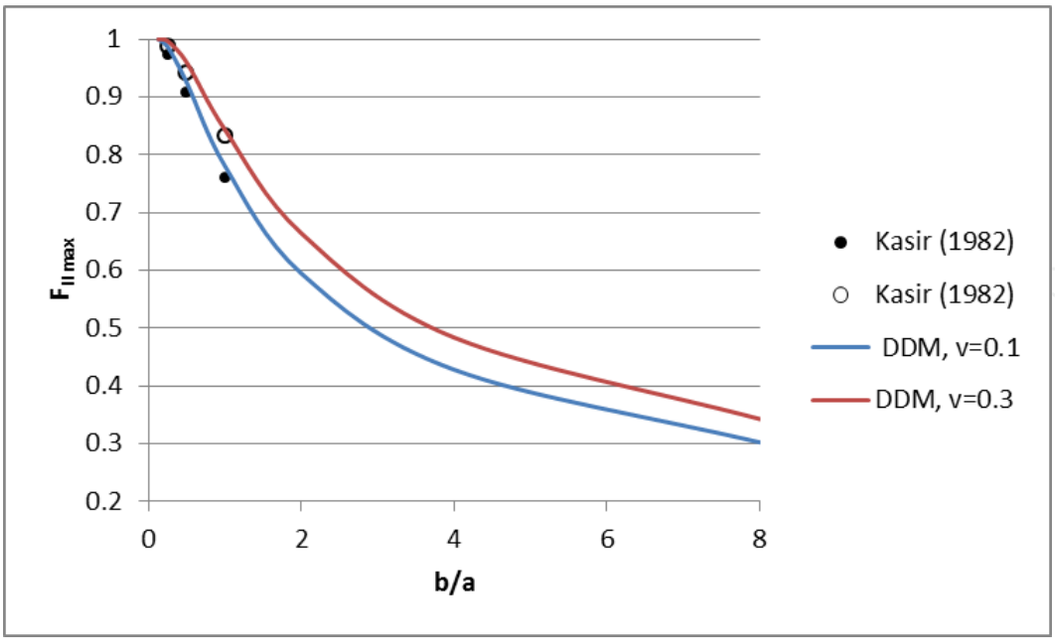

Figure 12. Effect of Poisson's ratio on Mode II dimensionless stress intensity factor for a rectangular crack in an infinite space.

3.2. Elliptical crack

For an elliptical crack embedded in an infinite body, the stress intensity factor variation along the crack edge can be obtained from the following analytical solution [36]:

$$K_I(\theta) = \frac{\sigma_n(\pi b)^{\frac{1}{2}}}{E(k)} \left(\frac{\sin^2\theta + \frac{b^4}{a^4}\cos^2\theta}{\sin^2\theta + \frac{b^2}{a^2}\cos^2\theta} \right)^{\frac{1}{4}} \tag{7}$$

where:

$\theta = \tan^{-1}\frac{y}{x}$, $\frac{x^2}{a^2} + \frac{y^2}{b^2} = 1$ and,

$E(k) = \int_0^{\frac{\pi}{2}} (1 - k^2 \sin^2\theta) d\theta$ *and* $k = 1 - \frac{b^2}{a^2}$

$E(k)$is the complete elliptical integral of the second kind while a is the major axis and $b$is the minor axis of ellipse. The maximum and minimum stress intensity factor at the end of minor and major axes, respectively, can be calculated using Equations 8a and 8b:

$$(K_I)_{max} = K_I\left(\theta = \frac{\pi}{2}\right) = \frac{\sigma_n\sqrt{\pi b}}{E(k)} \quad a$$
$$(K_I)_{min} = K_I(\theta = 0) = \frac{\sigma_n\sqrt{\pi b}}{E(k)}\sqrt{\frac{b}{a}} \quad b \tag{9}$$

Figure 13a and b show dimensionless stress intensity factor variation along the elliptical crack front using analytical solutions and DDM numerical modeling. Totally 154 DD elements were used in the model depicted in Figure 13a, and 628 elements in Figure 13b. Whereas SIF is proportional to the area of planar crack, the area of boundary element mesh in both cases is almost equal to the area of the modeled ellipse. For both models, the aspect ratio of the ellipse is $\frac{b}{a}=2$ and $F_1=\frac{K_1(\theta)}{\sigma_n(\pi b)^{\frac{1}{2}}}$. Both figures show that the trend of stress intensity factor variation can be appropriately modeled by DDM. Oscillation in SIF is because of stepwise mesh boundary used to define the geometry of the ellipse using rectangular elements. However, by using the average of SIF of the neighboring circumferential elements, the accuracy improves for both models and the maximum error decreases from about 24% to 9% for the first model and from 28% to 10% for the second model, as compared to the analytical solution in [36]. Using 20 elements along the major axis and 10 along the minor axis of the ellipse results in good agreement for F1 at $\theta=0$ and $\frac{\pi}{2}$(Figure 13-a). For $\theta\geq 60^{\circ}$, the rectangular mesh deviates less from the ellipse, and the error in dimensionless stress intensity factor is non-oscillatory and small. Increasing the number of elements doesn't improve the accuracy (Figure 13-b).

3.3. Penny-shaped crack

Stress intensity factor at the tip of a circular crack of radius $a$in an infinite solid under uniaxial tension σ_n is [46]:

$$\frac{2}{\pi}\sigma_n\sqrt{\pi a} \tag{10}$$

where:

$\theta=\tan^{-1}\frac{y}{x}$, $x^2+y^2=a^2$

Two different size meshes were considered to calculate dimensionless stress intensity factor variation along the tip of a circular crack as depicted in Figures 14a and 14b. The first model includes 76 elements and the second one has 308 elements. According to Figure 7, for a rectangular crack using 9×9 elements, the error in stress intensity factor is about 3 percent. For the penny-shaped crack, as with the elliptical crack, the error is a strong function of location. Because of the symmetry, error calculations are shown only for one eighth of the circle. The main reason of error in stress intensity factor along the crack front is jagged geometrical definition of the circle by using rectangular displacement discontinuity elements. The error in SIF can reach up to 20% along the crack front; however, the results are better for $\theta=0\ or\ \frac{\pi}{2}$- about 2.5% for the coarser model and almost zero for the finer model. Figure 15 compares F_1variation along the quarter front of the penny-shaped crack for two DD models as well as analytical solution. The figure shows the finer mesh helps to increase the accuracy where the crack front is straight, but is not helpful where

http://dx.doi.org/10.5772/56308

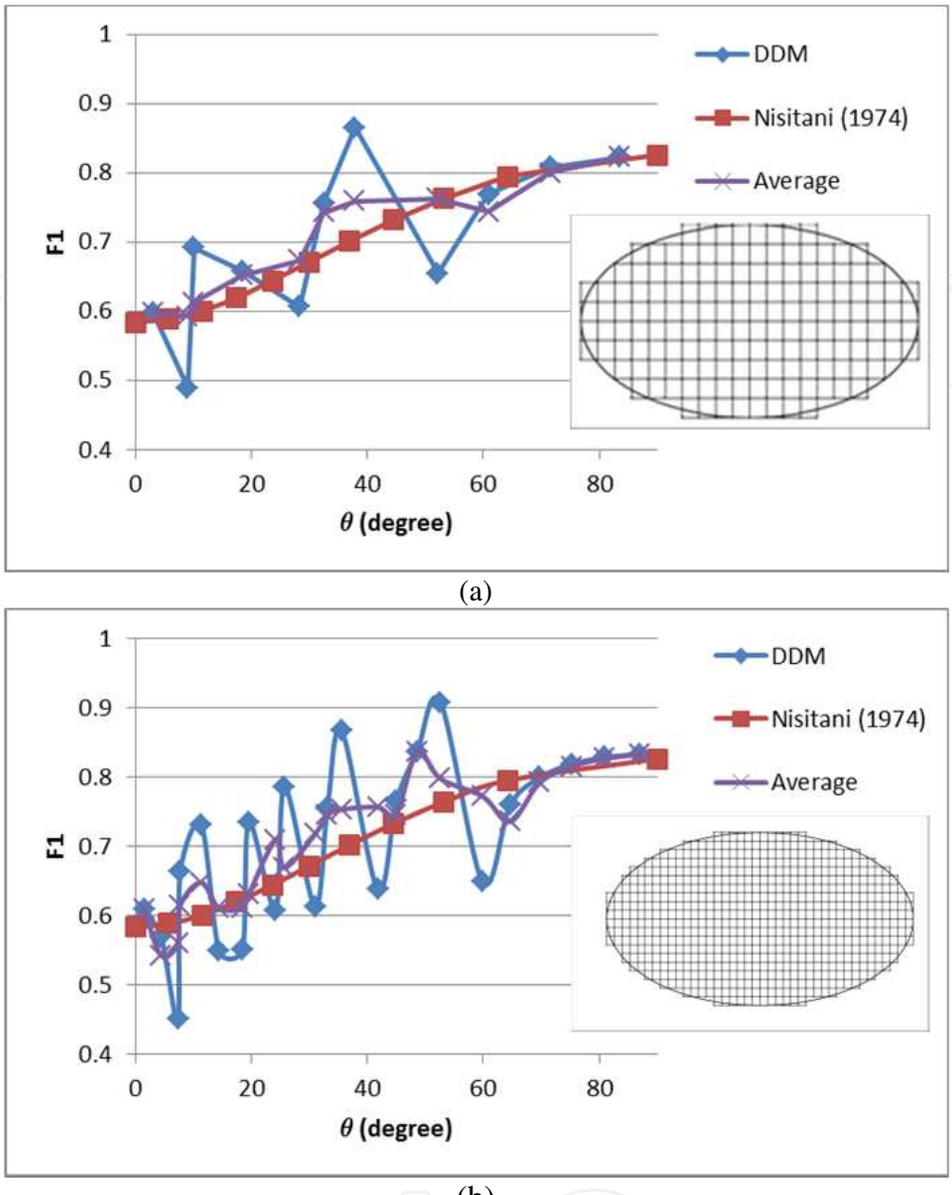

Figure 13. a. Dimensionless SIF variation along an elliptical crack front using analytical solution and DDM $\left(\frac{b}{a}=2.0\right)$, model No. 1 including 154 elements; b. Dimensionless SIF variation along an elliptical crack front using analytical solution and DDM $\left(\frac{b}{a}=2.0\right)$, model No. 2 including 628 elements

the crack front is stepwise. Similar to elliptical cracks, using the average SIF of neighbor circumferential elements considerably increases the accuracy of SIF distribution along the crack front of the penny-shaped discontinuity.

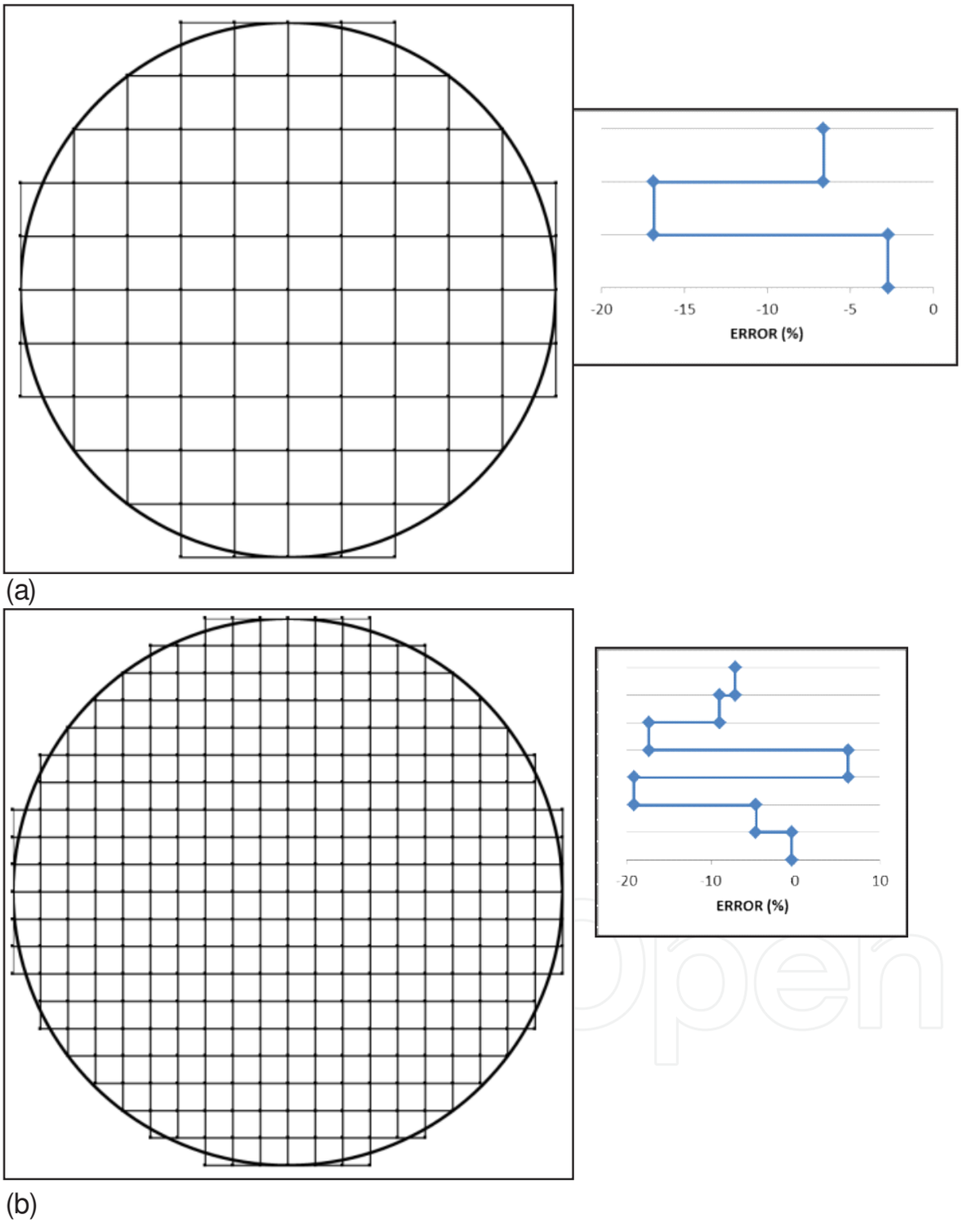

Figure 14. a Error in dimensionless calculation along a penny-shaped crack front, Model 1 including 76 elements; b. Error in dimensionless calculation along a penny-shaped crack front, Model 2 containing 308 elements

http://dx.doi.org/10.5772/56308

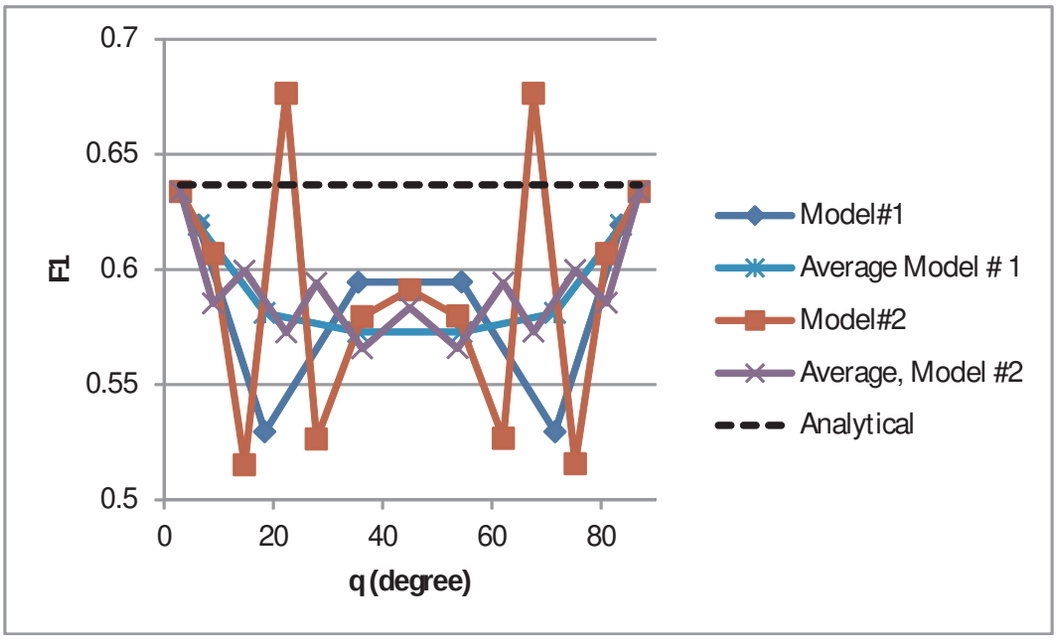

Figure 15. Comparison between dimensionless SIF for two DDM models with analytical solution of a penny-shaped crack stress intensity factor

4. Fracture propagation

For vertical fractures, lateral kinking propagation is modeled based on maximum circumferential stress criteria [47], which states growth should occur at the crack tip along a radial path perpendicular to the direction of greatest tension:

$$\tan\frac{\theta_0}{2}=\frac{1}{4}\left[\frac{K_I}{K_{II}}-Sgn\left(K_{II}\right)\sqrt{\left(\frac{K_I}{K_{II}}\right)^2+8}\right] \quad a$$
$$K_{eq}=K_I\cos^3\frac{\theta_0}{2}-\frac{3}{2}K_{II}\cos\frac{\theta_0}{2}\sin\frac{\theta_0}{2} \quad b \tag{11}$$

where θ_0 is the angle of kinking and $Sgn(K_{II})$denotes the sign of K_{II}. Equation 10-a is used to calculate the equivalent opening mode stress intensity factor in the direction of crack extension (K_{eq}) as in formula (10b).

Our model takes into account the height growth as pure Mode I propagation. Any contribution of Mode III or out of plane shear on vertical propagation is neglected; however, the possibility of fringe crack generation based on Mode I+III combination will be studied by Mode III SIF evaluation along the upper front of the fracture. The angle of twisting is dependent on the magnitude of Mode III and Mode I SIF as well as mechanical properties [48] and can be calculated using Equation 11. Higher values of Mode III SIF (or lower opening mode) result in bigger twisting angle.

$$\alpha=\frac{1}{2}\tan^{-1}\left[\frac{K_{III}}{K_I\left(1/2-\right)}\right] \tag{12}$$

Fracture front propagation velocity defines which edge extends first. Charles power law [49] was used to relate the equivalent opening Mode stress intensity factor at the tip of the crack to the propagation velocity as the following [49]:

$$V=AK_{eq}^{n} \tag{13}$$

5. Application: Fracture misalignment and height growth

Figure 16 shows the ideal alignment of horizontal well and longitudinal hydraulic fracture system where the horizontal well is perpendicular to the minimum remote horizontal stress $S_{hmin}=S_3$ and the wellbore lies in the principal remote stress plane, parallel to $S_{Hmax}=S_2$. However, hydraulic fractures may not necessarily start perpendicular to the minimum horizontal remote stress because of the lack of alignment between the wellbore and the principal stresses, local stress perturbation, or natural fracture adjacent to a horizontal well [50]. The geometry of a hydraulic fracture could be further complicated by lateral propagation which is non-planar and height growth that is non-uniform. The non-planarity of the fracture path and its resultant near-wellbore width restriction and excessive treating pressure were considered by [51] and [52] using 2-D and pseudo 3-D displacement discontinuity modeling, respectively. In this paper, we study the effect of misalignment angle on the possibility of irregular height growth as well as fringe fracture generation by contemplating the stress intensity factor distribution around the periphery of misaligned hydraulic fracture. Wellbore stress effects are not considered in this study.

http://dx.doi.org/10.5772/56308

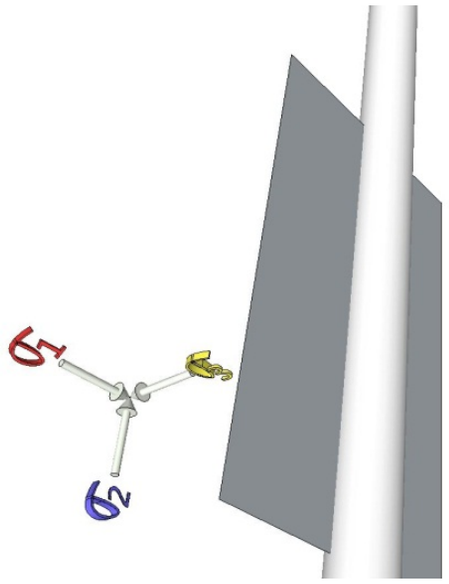

Figure 16. Ideal longitudinal fractured horizontal well with hydraulic fracture perpendicular to σ_{hmin}.

For the propagation cases that follow, we assume $S_{hmin} = S^r_{xx} = 15$ MPa (where r denotes remote stresses), P_{frac} is constant and equal to 20.0 MPa, the remote compression differential stress is $(\sigma^r_{yy} - \sigma^r_{xx}) = 2.0\ MPa$, the propagation velocity exponent is $n = 2$, $\nu = 0.25$ and $E = 30.0\ GPa$. The initial fracture length and height are assumed to be 3 meters (a square crack), subdivided by 9 DDM elements. The fracture is assumed to remain rectangular during the propagation (i.e., the height is uniform along the entire length, but the crack path in plan-view can be non-planar).

To examine the effect of horizontal well misalignment angle on fracture propagation (Figure 17), first we assume the differential compression in y direction $(S^r_{yy} - S^r_{xx})$ is 40% of the net injection pressure $(P_{frac} - S^r_{xx})$. Fracture path non-planarity is strongly affected by the initial misalignment angle, β, especially for extreme cases. The starter fracture is centered at (0,0) and is rotated counterclockwise by β. The smallest misalignment $\beta = 10°$ is the closest to planar fracture and $\beta = 89°$ is the most curved path.

Nonplanar propagation has an impact on height growth (Figures 18 and 19). For the smaller misalignment cases (β <=45º), crack height keeps pace with crack length growth for our imposed rectangular shape (Figure 18). For our stronger misalignment cases of β >45º, the crack height growth is somewhat hindered to only ~80% of the length. Looking at the opening mode SIF (K_I) distribution along the top edge of the fracture is more interesting, however, since our propagation algorithm responds only to the average crack tip SIF. The more severe the fracture reorientation, the lower the K_I for the initial fracture segment, where for the 89º misalignment case, the K_I at the center of the crack is 50% lower than it would be for a planar fracture. This implies that at the wellbore, there could be a restriction in fracture height because of the non-planar propagation that might also restrict width and hinder infectivity.

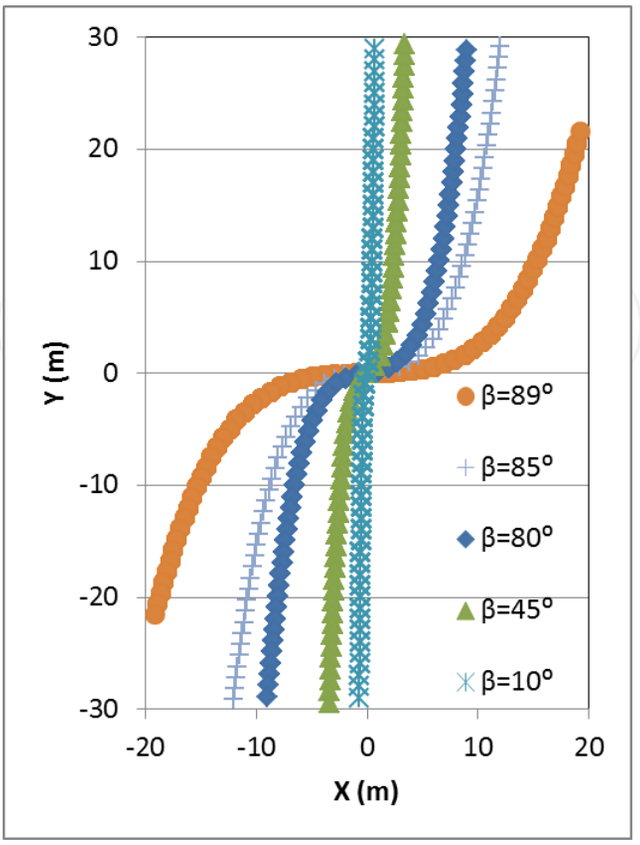

Figure 17. Map view of non-planar fracture paths (upper front propagation, $\frac{\Delta H}{2} = 25.0\ m$)

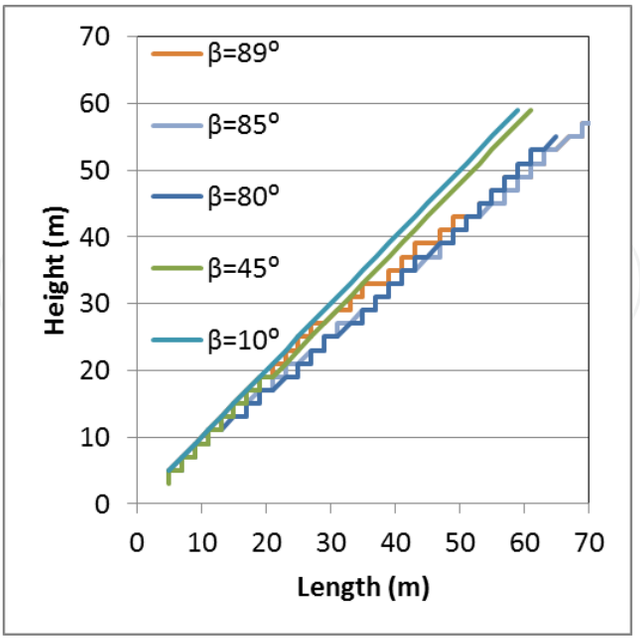

Figure 18. Vertical versus lateral growth of the hydraulic fracture

http://dx.doi.org/10.5772/56308

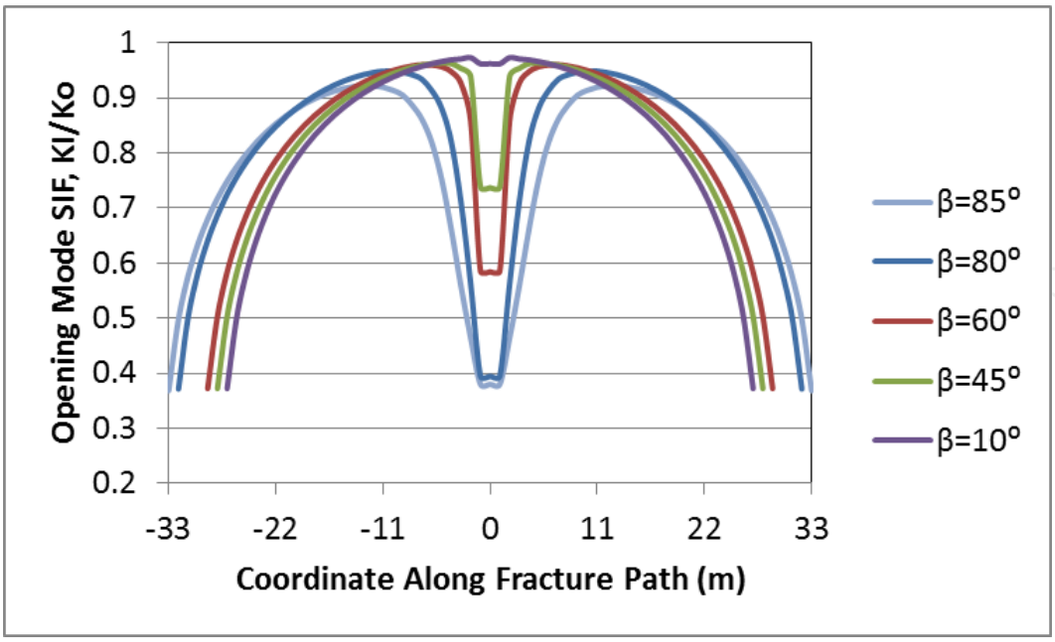

Figure 19. K_I along the upper front of hydraulic fracture implying height growth restriction around the wellbore due to misalignment normalized to SIF of planar fracture at $x=0$(upper front propagation, $\frac{\Delta H}{2}=25.0\ m$)

The time progression of the K_I variation along the top fracture front is displayed in Figure 20 for the case $\beta=80°$. The K_I at the initial fracture location (the injection location) grows very slowly in comparison to the curving wings of the fracture.

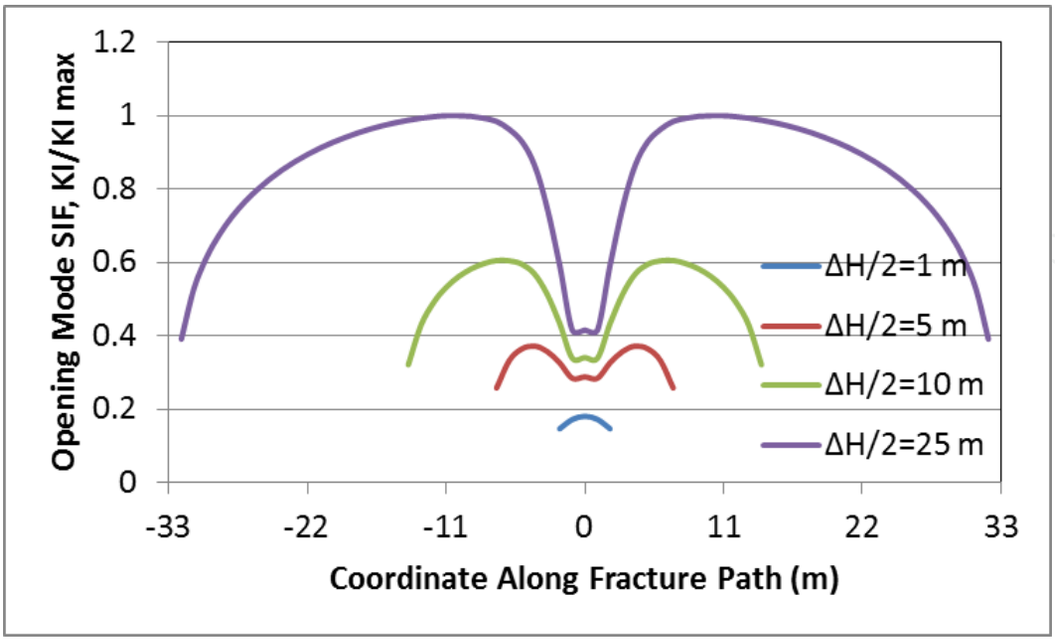

Figure 20. K_I distribution variation normalized by the absolute maximum opening mode SIF during propagation along the upper front of a hydraulic fracture perforated from a misaligned horizontal wellbore. Misalignment angle, $\beta=80°$.

Although K_I is restricted in the misaligned portion of the fracture, Mode III or out of plane shear SIF(K_{III}) is accentuated. This twisting SIF could cause the fracture to break down into several en echelon cracks, causing further propagation hindrance in the vertical direction. Figure 21 depicts the distribution of K_{III} for varying fracture misalignment based on the simulation of Figure 19.

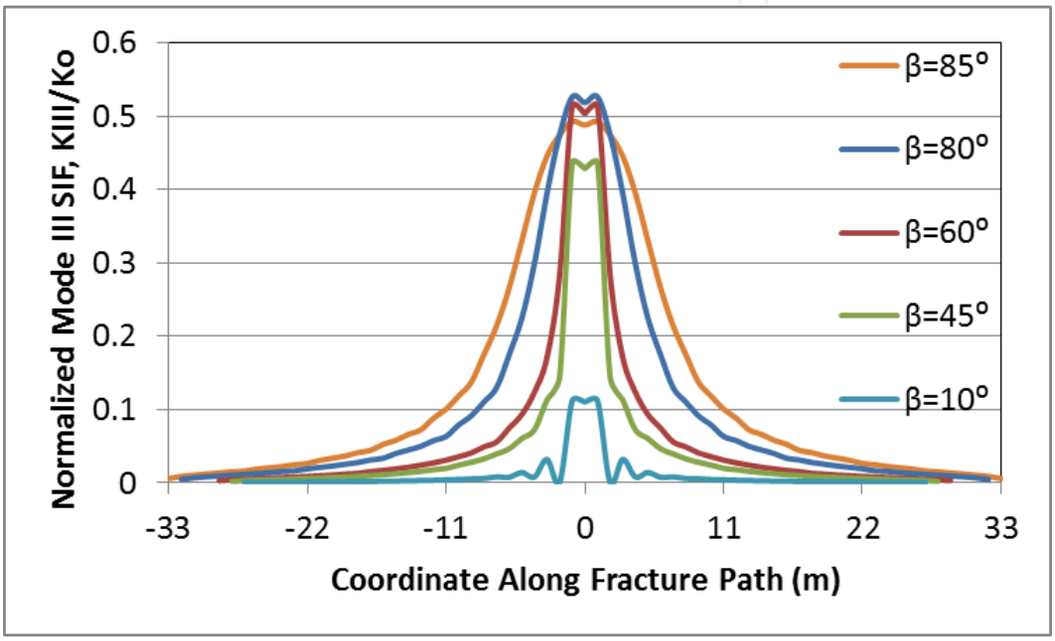

Figure 21. Mode III SIF along the upper front of hydraulic fracture normalized to SIF of planar fracture at $x=0$, implying height growth restriction around the wellbore due to misalignment (upper front propagation, $\frac{\Delta H}{2}=25.0\ m$)

Fracture path is affected by remote stresses as well as near-tip stress distribution and is quantifies by ratio R[53] assuming compression is positive:

$$R=\frac{(\sigma_{Hmax}-\sigma_{hmin})}{(P_{frac}-\sigma_{hmin})}=\frac{(\sigma^{r}_{yy}-\sigma^{r}_{xx})}{(P_{frac}-\sigma^{r}_{xx})} \tag{14}$$

The magnitude of Rshows how fast the misaligned fracture will be aligned with maximum horizontal stress. Figure 20 present the bigger the magnitude of Rratio, the faster the fracture will be rotated to be aligned perpendicular to minimum horizontal stress. Because the differential remote stress is kept constant for these 3 cases, smaller magnitude of ratio Rmeans the dominance of fracture driving stresses results in a straighter fracture path.

http://dx.doi.org/10.5772/56308

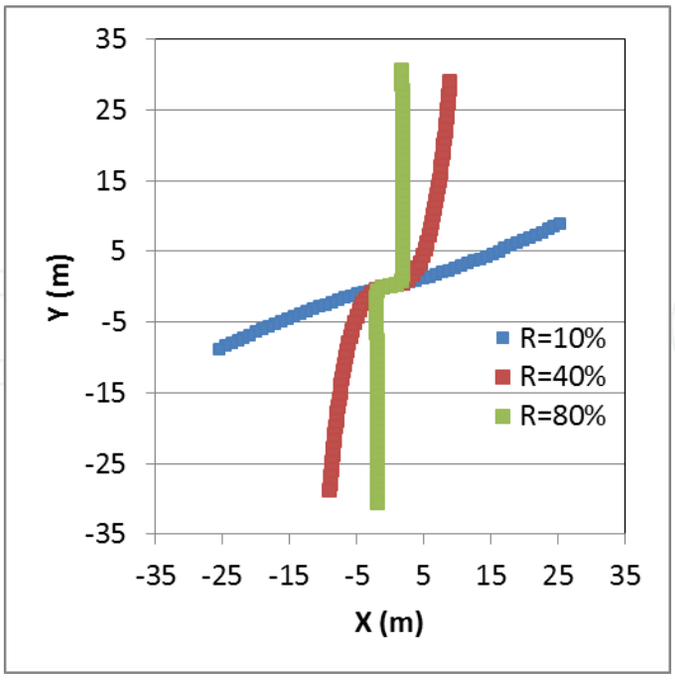

Figure 22. R ratio effect on fracture path. Upper front propagation, $\frac{\Delta H}{2} = 25.0\ m$, $\beta = 80°$ and $(\sigma^r_{yy} - \sigma^r_{xx}) = 2.0\ MPa$.

6. Conclusion

Numerical methods are necessary for the SIF evaluation of 3-D planar cracks because analytical solutions are limited to simple geometries with special boundary conditions. In this paper, the capability of DDM using constant rectangular discontinuity elements and considering the empirical constant proposed by Olson (1991) was satisfactory examined for cracks with simple geometry. The accuracy of the model is excellent especially for rectangular and square shaped cracks. The stepwise shape of the mesh boundary when representing elliptical or penny-shaped cracks introduces more error in to the calculation, but the minimum and maximum SIF values can be accurately computed.

Acknowledgements

Funding for this project is provided by RPSEA through the "Ultra-Deepwater and Unconventional Natural Gas and Other Petroleum Resources" program authorized by the U.S. Energy Policy Act of 2005. RPSEA (www.rpsea.org) is a nonprofit corporation whose mission is to provide a stewardship role in ensuring the focused research, development and deployment of safe and environmentally responsible technology that can effectively deliver hydrocarbons from domestic resources to the citizens of the United States. RPSEA, operating as a consortium of premier U.S. energy research universities, industry, and independent research organiza-

tions, manages the program under a contract with the U.S. Department of Energy's National Energy Technology Laboratory. Authors gratefully appreciate RPSEA for providing the funding for this work.

Author details

Farrokh Sheibani* and Jon Olson*

*Address all correspondence to: sheibani@utexas.edu

*Address all correspondence to: jolson@austin.utexas.edu

University of Texas at Austin, Austin, USA

References

[1] Okada, Y. Internal deformation due to shear and tensile faults in a half-space. Bulletin of the Seismological Society of America (1992). , 82(2), 1018-1040.

[2] Olson, J. E. Fracture mechanics analysis of joints and veins. PhD Dissertation. Stanford University; (1991).

[3] Cahng, C. C, & Mear, M. E. A Boundary Element Method for Two Dimensional Linear Elastic Fracture Analysis. International Journal of Fracture (1995). , 74-219.

[4] Pollard, D. D, & Segall, P. Theoretical displacement and stress near fracture in rock: with application to faults, joints, veins, dikes and solution surfaces. In: Atkinson BK. (ed.) Fracture Mechanics of Rock. London: Academic Press; (1987). , 277-350.

[5] Irwin, G. R. Analysis of stress and strain near the end of a crack traversing a plate. Journal of Applied Mechanics (1957). , 24-361.

[6] Chan, S. K, Tuba, I. S, & Wilson, W. K. On the finite element method in linear fracture mechanics. Engineering Fracture Mechanics (1970). , 2-1.

[7] Henshell, R. D, & Shaw, K. G. Crack tip finite elements are unnecessary. International Journal for Numerical Methods in Engineering (1975). , 9-495.

[8] Barsoum, R. S. On the use of isoparametric finite elements in linear fracture mechanics, International Journal for Numerical Methods in Engineering (1976). , 10(1), 65-88.

[9] Benzley, S. E. Representation of singularities with isoparametric finite elements., International Journal for Numerical Methods in Engineering (1974). , 8(3), 537-545.

[10] Tarancon, J. E, Vercher, A, Giner, E, & Fuenmayor, F. J. Enhanced blending elements for XFEM applied to linear elastic fracture mechanics. International Journal for Numerical Methods in Engineering (2009). , 77(1), 126-148.

[11] Jiang, S, Ying, Z, & Du, C. The optimal XFEM approximation for fracture analysis. IOP Conference Series: Materials Science and Engineering (2010).

[12] Lin, X, & Ballmann, J. Re-consideration of Chen's problem by finite difference method. Engineering Fracture Mechanics (1993). , 44(5), 735-739.

[13] Chen, Y. M. Numerical computation of dynamic stress intensity factors by a Lagrangian finite-deference method (THE HEMP CODE). Engineering Fracture Mechanics (1975).

[14] Pande, G. N, Beer, G, & Williams, J. R. Numerical Methods in Rock Mechanics. West Sussex: John Wiley & Sons Ltd; (1990).

[15] Rizzo, F. J. An integral equation approach to boundary value problems of classical elastostatics. Quarterly of Applied Mathematics (1967). , 25-83.

[16] Crouch, S. L. Solution of plane elasticity problems by the displacement discontinuity method. International Journal for Numerical Methods in Engineering (1976). , 10(2), 301-343.

[17] Crouch, S. L, & Starfield, A. M. Boundary element methods in solid mechanics. London: George Allen & Unwin; (1983).

[18] Schultz, R. A. Stress intensity factor for curved cracks obtained displacement discontinuity method. International Journal of Fracture (1988). RR34., 31.

[19] Aydin, A, & Schultz, R. A. Effect of mechanical interaction on the development of strike-slip faults with echelon patterns. Journal of Structural Geology (1990). , 12(1), 123-129.

[20] Crawford, A. M, & Curran, J. H. Higher-order functional variation displacement discontinuity elements. International Journal of Rock Mechanics and Mining Sciences & Geomechanics Abstract (1982). , 19(3), 143-148.

[21] Scavia, C. The displacement discontinuity method on the analysis of open cracks. Meccanica (1991). , 26(1), 27-32.

[22] Yan, X. Stress intensity factors for cracks emanating from a triangular or square hole in an infinite plate by boundary elements. Engineering Failure Analysis (2005). , 12(3), 362-375.

[23] Shou, K. J, & Crouch, S. L. A higher order displacement discontinuity method for analysis of crack problems. International Journal of Rock Mechanics and Mining Sciences & Geomechanics Abstract (1995). , 32(1), 49-55.

[24] Dong, C. Y, & Pater, C. J. Numerical implementation of displacement discontinuity method and its application in hydraulic fracturing. Computer Methods in Applied Mechanics Engineering (2001).

[25] Wen, P. H, Aliabadi, M. H, & Rooke, D. P. A fictitious stress and displacement discontinuity method for dynamic crack problems. In: Brebbia CA. (ed.) Boundary Element Method XVI. Southampton: Computational Mechanics Publications; (1994). , 469-476.

[26] Thomas, A. L, & Pollard, D. D. The geometry of echelon fractures in rock-implication from laboratory and numerical experiments. Journal of Structural Geology (1993).

[27] Kattenhorn, S. A. A. D mechanical analysis of normal fault evolution and joint development in perturbed stress field around normal faults. PhD Dissertation. Stanford University; (1998).

[28] Willemse EJMPollard DD. Normal Fault growth: Evolution of tipline shapes and slip distribution. In: Lehner FK, Urai JL. (ed.) Aspects of Tectonic Faulting. Newyork: Springer; (2000). , 193-226.

[29] Olson, J. E. Fracture aperture, length and pattern geometry development under biaxial loading: a numerical study with application to natural, cross-jointed systems. Geological Society Special Publication (2007). , 289-123.

[30] Mériaux, C, & Lister, J. R. Calculation of dyke trajectories from volcanic centers. Journal of Geophysical Research (2002). B4) 2077-2087.

[31] Mutlu, O, & Pollard, D. D. (2006). A complementarity approach for modeling fractures. In: Yale D, Holtz S, Breeds C, and Ozbay U. (eds.) 50 years of Rock Mechanics-Landmarks and Future Challenges: The 41st U.S. Symposium on Rock Mechanics, Paper No: ARMA/USRMS June 17-21 2006, Golden, CO, USA., 06-1058.

[32] Ritz, E, & Pollard, D. D. Closure of circular arc cracks under general loading: effects on stress intensity factors. International Journal of Fracture (2011). , 167(1), 3-14.

[33] Murakami, Y, & Endo, M. Quantitative evaluation of fatigue strength of metals containing various small defects or cracks. Engineering Fracture Mechanics (1983). , 17(1), 1-15.

[34] Murakami, Y, Kodama, S, & Konuma, S. Quantitative evaluation of effects of non-metallic inclusions on fatigue strength of high strength steels. I: Basic fatigue mechanism and evaluation of correlation between the fatigue fracture stress and the size and location of non-metallic inclusions. International Journal of Fatigue (1989). , 11(5), 291-298.

[35] Irwin, G. R. (1962). Crack-extension force for a part-through crack in a plate. Journal of Applied Mechanics 1962;, 29(4), 651-654.

[36] Nisitani, H, & Murakami, Y. Stress intensity factor of an elliptical crack and semi-elliptical crack in plates subjected to tension. International Journal of fracture (1974). , 10(3), 353-368.

[37] Weaver, J. Three dimensional crack analysis. International Journal of Solids and Structures (1977). , 13(4), 321-330.

[38] Kassir, M. K. rectangular crack subjected to shear loading. International Journal of Solids and Structures 1982;, 18(12), 1075-1082.

[39] Isida, M, Yoshida, T, & Noguchi, H. A rectangular crack in an infinite solid, a semi-infinite solid and a finite-thickness plate subjected to tension. International Journal of Fracture (1991). , 52-79.

[40] Wang, Q, Noda, N. A, Honda, M. A, & Chen, M. Variation of stress intensity factor along the front of a 3D rectangular crack by using a singular integral equation method. International Journal of Fracture (2001). , 108-119.

[41] Kassir, M. K. Stress intensity factor for a three-dimensional rectangular crack. Journal of Applied Mechanics (1981). , 48(2), 309-313.

[42] Noda, N. A, & Kihara, T. A. Variation of the stress intensity factor along the front of a D rectangular crack subjected to mixed-mode load. Archive of Applied Mechanics (2002). , 3.

[43] Mastrojannis, E. N, Keer, L. M, & Mura, T. A. Stress intensity factor for a plane crack under normal pressure. International Journal of Fracture (1979). , 15(3), 101-114.

[44] Olson, J. E. Sublinear scaling of fracture aperture versus length: An exception or the rule. Journal of Geophysical Research (2003). B9) 2413-2424.

[45] Mear, M. E, & Rodin, G. J. An isolated Mode I three-dimensional planar crack: The stress intensity factor is independent to elastic constant. International Journal of Fracture (2011). , 172(2), 217-218.

[46] Sneddon, I. N. The distribution of stress in the neighborhood of a crack in an elastic solid. Proceedings of the Royal Society of London. Series A, Mathematical and Physical Sciences (1946). , 187(1009), 229-260.

[47] -Erdogan, F, Sih GC. On the crack extension in plates under plane loading and transverse shear. ASME Journal of Basic Engineering 1963;85 519-527

[48] Pollard, D. D, Segall, P, & Delaney, P. T. Formation and interpretation of dilatant echelon cracks. Geological Society of America Bulletin (1982). , 93-1291.

[49] Atkinson, B. K. Subcritical crack growth in geological materials. Journal of geophysical research (1984). B6) 4077-4114

[50] Olson, J. E. Multi-fracture propagation modeling: Application to hydraulic fracturing in shales and tight gas sands. The 42st U.S. Symposium on Rock Mechanics and 2nd

U.S.-canada Rock Mechanics Symposium, Paper No: ARMA June 29-July 2 (2008). San Francisco, CA, USA., 08-327.

[51] Olson, J. E. Fracturing from highly deviated and horizontal wells: Numerical analysis of non-planar fracture propagation. SPE Rock Mountain Regional/Low Permeability Reservoir Symposium, Paper No. SPE 29573, March (1995). Denver, CO, USA., 20-22.

[52] Olson, J. E, & Wu, K. Sequential versus simultaneous multi-zone fracturing in horizontal wells: Insight from a non-planar, multi-frac numerical model. SPE Hydraulic Fracturing Technology Conference, Paper No: SPE PP, February 6-8 (2012). The Woodland, TX, USA., 152602.

[53] Cruikshank, K. M, Zhao, G, & Johnson, A. M. Analysis of minor fractures associated with joints and faulted joints. Journal of Structural Geology (1991). , 13(8), 865-886.